Photoactivity properties of ZnO doped with cerium ions: an EPR study

Photoactivity properties of ZnO doped with cerium ions: An EPR study

1. Introduction

Transition metal oxides with nanostructures have attracted considerable interest in many areas of chemistry, physics, and materials science. Compared to other metal oxide nanomaterials, zinc oxide (ZnO) displays novel nanostructures. ZnO could be considered as an alternative to TiO_2 in photo-catalysis[1], optics and solar cells, due to its abundance[2, 3], high physical and chemical stability, low cost, non- toxicity, high electron mobility, low crystallization temperature and simple synthesis. It has a wide band gap (3.37 eV) and a large exciton binding energy (60 meV). [4]

ZnO exhibits the hexagonal (wurtzite) crystal structure with a = 3.25 Å and c = 5.12 Å. The Zn atoms are tetrahedrally coordinated to four O atoms, where the Zn d-electrons hybridize with the O p-electrons. Layers occupied by zinc atoms alternate with layers occupied by oxygen atoms.
The optical properties of ZnO, studied using photoluminescence, photoconductivity, and absorption spectroscopies, reflect the intrinsic direct bandgap, a strongly bound exciton state, and gap states due to point defects. The intrinsic defect levels that lead to n-type doping in pristine ZnO lay approximately 0.01–0.05 eV below the conduction band and have been attributed to interstitial Zinc atoms (Zn_i), oxygen vacancies (V_O), or trapped atomic hydrogen introduced during growth[5]. Nanoscale ZnO materials showed higher photocatalytic activity than the bulk materials due to their larger surface area and larger number of active sites.

Many works in literature report that metal ion doping can modify the surface properties of ZnO, hinder the recombination of photo-generated electron-hole pairs and increase the amount of the active sites. In particular the photocatalytic activity of ZnO can be significantly enhanced by doping with lanthanide ions having $4f^x$ configuration [6]. Indeed, lanthanides are able to trap electrons. This phenomenon can effectively reduce the recombination of photo-generated electron-hole pairs, resulting in an improved photo-oxidation ability of the system (driven by reactive holes). Various research groups reported for Ln-doped ZnO higher photocatalytic activity than for pure ZnO, including Eu [7, 8] [22][9], La [10, 11] and Ce [12]. In particular, the (Ce^{3+}/Ce^{4+}) redox pair could act as an electron scavenger that traps the bulk electrons in semiconductor modifying the band gap [13]. In structural terms, due to both the huge difference in size of the Zn^{2+} and Ce^{4+} ions, the different crystal structure of the two oxides and the different valence of the ions, the insertion of cerium ions in the lattice of ZnO is highly improbable [12, 14, 15]. The enhancement of the

photocatalytic activity of the doped samples should therefore be due to the electron transfer at the interfaces between different crystalline structures [14, 16].

In the recent past, an additional role of cerium doping has highlighted by our group, namely the capability to sensitize a wide band oxide to the visible light. This has been observed in the case of Ce doped zirconium dioxide, a system that, in spite of the ZrO_2 band gap of about 5 eV, becomes visible light sensitive with the introduction of Ce ions [17]. Even if, at variance with the system here described, in the case of Ce/ZrO_2 the doping Ce^{4+} ions are diluted into the oxide matrix, it is worth of exploring if some activity of cerium in promoting visible light sensitisation is obtained also in the case of ZnO. The data reported in literature for the Ce doped ZnO system are very heterogeneous. Some authors claim that cerium ions enter in the ZnO lattice, influencing the lattice parameters of the oxide [18]; others that cerium segregates forming a new phase, influencing the particle size and particle growth of the ZnO matrix [7]. In general, none of them explains the role of cerium in promoting the photo activity of the samples[C1].

Based on the above concerns, this work reports on the features of Ce doped ZnO nanoparticles (CZ), with two different cerium loading (1 and 10% molar), that we prepared by a simple chemical precipitation route without any organic solvent[C2] or surfactant. We characterized the prepared ZnO-based materials by different techniques and we tested their photo-activity in the visible range monitoring the formation of OH reactive radicals under polychromatic irradiation with $\lambda > 420$nm. To measure the amount of photo formed radicals the spin trapping technique was used based on the detection, by Electron Paramagnetic Resonance (EPR), of stable radical adducts formed via reaction of $OH^{\bullet}$ radicals with molecules of the DMPO spin probe.

2. Experimental

2.1 Samples preparation

We used a precipitation method to prepare bare and cerium doped ZnO, with surface area larger than that reported for classical synthesis of ZnO [19]. In a typical synthesis, 2.2g of $Zn(CH_3COO)_2 \cdot 2H_2O$ (Sigma Aldrich XX%) are dissolved into 160 ml of bi-distilled water and 80 ml of ethanol: the solution is kept under magnetic stirring for 1 hour at room temperature. Then, 160 ml of a 1M NaOH aqueous solution is added dropwise, allowing the precipitation. Then, the solution is kept stationary for 48 hours. Finally, the solution is filtered, washed and dried at 70°C for 12 hours. The final product is obtained after calcination at 300°C for 30 hours in air.

To prepare the cerium doped samples, the stoichiometric amount (0.038 g and 0.38 g) $CeCl_3 \bullet 7H_2O$ (Sigma Aldrich 99.99%) is added to the starting solution in order to obtain samples with 1 and 10% molar loading. The materials will be hereafter labeled ZnO, CZ1 and CZ10 respectively.

2.2 Samples characterization

Powder X-rays diffraction (XRD) patterns were recorded with a PANalytical PW3040/60 X'Pert PRO MPD using a copper K_α radiation source (0.154056 nm). The signals were scanned continuously in the 2θ ranges between 20° and 80°. In order to identify the phases presented in the samples, the X'Pert High-Score software was employed. The Scherrer equation has been used to evaluate the crystallite size of the existing phases[C3].

The specific surface area measurements were carried out on a Micromeritics ASAP 2020 using the Brunauer-Emmett-Teller (BET) model on the N_2 adsorption measurement. Prior to the adsorption run, all the samples were outgassed at 573 K for two hours.

The UV-Vis absorption spectra were recorded using a Varian Cary 5000 spectrometer, equipped with an integration sphere for diffuse reflectance studies, using a Carywin-UV/scan software. A sample of Teflon with 100% reflectance was used as reference.

The sample optical band gap energies were calculated taking into account that the energy dependence of the absorption coefficient (α) for semiconductors in the region near the absorption edge is given by:

$$\alpha \propto \left(\frac{h\nu - E_{bg}}{h\nu}\right)^{\eta}$$

Where hν is the energy of the incident photon and E_{bg} is the optical absorption energy. η depends on the type of optical transition, in crystalline semiconductors is 1/2 (direct-allowed), 3/2 (direct-forbidden), 2 (indirect-allowed), and 3 (indirect-forbidden). As far as ZnO is concerned, this oxide shows a direct-allowed optical transition, with a value of 2 for η. Finally, since the scattering coefficient weakly depends on energy and $F(R_\infty)$ can be assumed proportional to the absorption coefficient within the narrow range of energy containing the absorption edge feature.

$$F(R_\infty) = \left(\frac{h\nu - E_{bg}}{h\nu}\right)^{\eta}$$

The plot $(F(R_\infty)*h\nu)^{1/\eta}$ vs hν can be thus used to determine the absorption edge energies and energy gaps.

X-band continuous wave (CW) EPR spectra of the solids in various conditions have been recorded on a Bruker EMX spectrometer equipped with a cylindrical cavity and operating at a 100 kHz field modulation. The measurements were carried out at the liquid nitrogen temperature (77 K) in quartz cells that can be connected to a conventional high-vacuum apparatus (residual pressure $<10^{-4}$ mbar). To investigate the redox behaviour of the materials a batch of the samples was thermally annealed at 570 K for one hour under vacuum condition before the EPR spectra acquisition.
The generation of radical species in solution was performed irradiating the samples with a 1000 W Xenon lamp (Oriel instruments) equipped with a IR water filter and then was monitored by the EPR-spin trapping technique using a Miniscope 100 spectometer from Magnettech and DMPO (5,5-dimethyl-1-pyrroline-N-oxide, Alexis Biochemicals, San Diego, CA) as spin trapping agent.

3. Results and discussion

3.1. Materials characterization

Figure 1 shows the X-ray diffraction patterns of the three samples prepared in this work. All the patterns show the peaks typical of the hexagonal wurtzite phase of ZnO (00-036-1451 ICDD pattern). Ce doping (for both loadings) leads to the formation of additional peaks. In particular, the peak at $2\Theta = 28.6°$ corresponds to the (111) planes of cubic ceria (00-034-0394 ICDD pattern) [20]. The introduction of cerium ions does not seem to influence much the ZnO wurtzite phase. Indeed, already for the sample containing 1% of dopant (CZ1) there's evidence for the formation of a separate phase (cubic ceria). Nevertheless, the presence of few Ce ions trapped into the lattice structure cannot be completely excluded.

Table 1 reports the average crystallite values obtained using the Scherrer equation and the specific surface areas measured by the BET method. The ZnO crystallites are quite small, but the CeO_2 crystallites are significantly smaller (about 4 nm). In agreement with the lower crystallite size, the doped materials also show a higher surface area than the bare one.

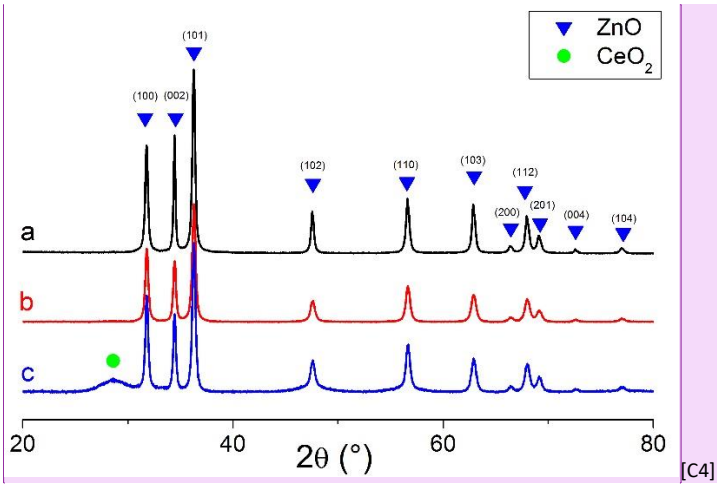

Figure 1: XRD patterns of (a) ZnO, (b) CZ1, (c) CZ10.

Table 1: Average crystallite size (*d*) obtained for the two phases from Scherrer analysis, BET surface area (SSA_{BET}) and energy gap (E_g) calculated with the Tauc plot

Sample	*d* ZnO (nm)	*d* CeO_2 (nm)	SSA_{BET} (m^2g^{-1})	E_g (eV)
ZnO	39±3	-	20±0.0535	3.278
CZ1	27±8	4.3±2	31±0.0644	3.273
CZ10	26±10	2.6±1	54±1.1090	3.256

We investigated the electronic structure of the materials by means of Diffuse Reflectance Spectroscopy (DRS). Figure 2 shows the Kubelka-Munk transformed diffuse reflectance spectra (which are proportional to the absorbance) obtained for bare and doped samples. The spectra are dominated by the valence band (VB) – conduction band (CB) transition occurring at about 370 nm, typical of the ZnO phase. Ce doping results in an increase in the overall absorption proportional to the amount of dopant. We calculated the energy gap (E_g) value for all samples using the Tauc plot. Energy gap values have been calculated by linearization of the plot reporting $(\alpha h\nu)^2$ vs $h\nu$ typical of direct band gap transitions [21] for ZnO and doped materials. The calculated E_g values for ZnO, CZ1 and CZ10 are 3.278, 3.273, 3.256 respectively and 2.9 eV for CeO_2 (table 1). The energy gap calculated for the three samples are very close one to each other, showing that doping did not cause a significant change in the electronic properties of the ZnO matrix. The effect related to Ce doping consists in the onset of an optical absorption in the visible region (roughly between 400 nm and 470 nm) which corresponds to the absorption shown by bare CeO_2 in the same region (Fig. 2d).

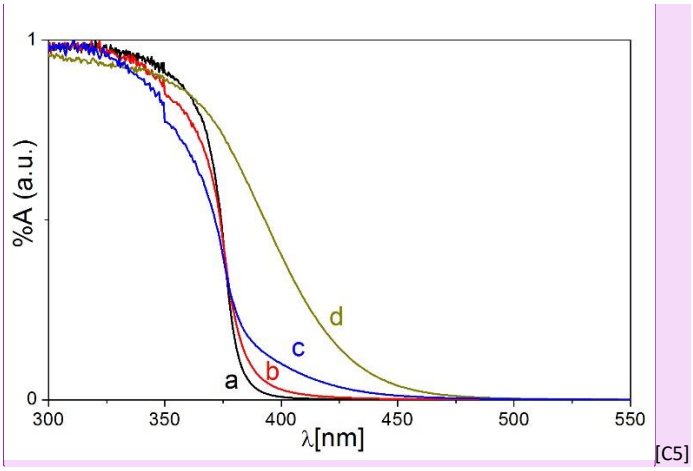

Figure 2: Absorbance (Kubelka-Munk transformed diffuse reflectance) spectra of (a) ZnO, (b) CZ1, (c) CZ10, (d) CeO_2

The bare and doped ZnO powders display EPR spectra characterized by a slightly asymmetric line with g_{av} =1.959 (Fig. 3a). This signal, widely reported in the literature, [22] is always present in native ZnO and has been assigned to shallow donor impurities [23]. No sign of any hyperfine interaction is detectable for this signal that is also present in doped materials but with a lower intensity. Furthermore, another non symmetric signal centred at about g=2.000 is also present in all the spectra. This one has been assigned to a hole defect generated during the synthesis process.

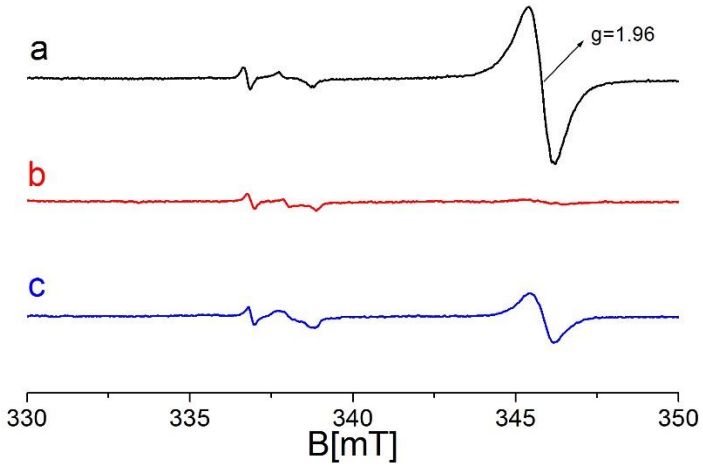

Figure 3. EPR spectra of as prepared samples a) ZnO, b) CZ1, c) CZ10

To compare the redox behaviour of the materials, a reducing thermal annealing under vacuum at 570K for 1 hour was performed on the samples. When the oxygen partial pressure in the atmosphere over the solid is decreased, even at moderate temperature, ZnO loses oxygen from

the lattice. This causes the simultaneous formation of oxygen vacancies and excess electrons in the reduced solid according to the following equation:

$$O_2^- + 2\ Zn^{2+} \rightarrow 1/2\ O_2 + V_O^{\bullet\bullet} + 2\ Zn_i^+$$

where the oxygen vacancy is indicated using the Kröger and Vink notation and is usually thought to be empty as excess electrons are stabilized under the form of paramagnetic interstitial Zn_i^+ ions [23]

The three samples behave differently when submitted to this treatment. Inded, only the sample CZ1 seems to be affected. In particular, the signal centred at g=1.96 increases its intensity of more than one order of magnitude. On the contrary, the same signal intensity decreases in bare ZnO and in CZ10. The defects in the region of g= 2.000 are not affected by the reduction process.

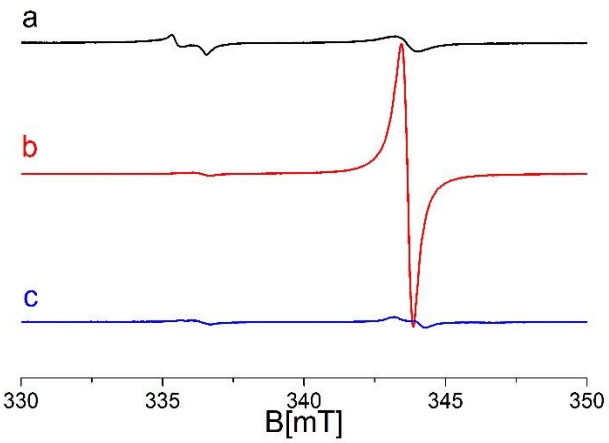

Figure 4. EPR spectra of reduced samples a) ZnO, b) CZ1, c) CZ10

When the reduced samples are contacted with molecular oxygen, an electron transfer from the surface to the oxygen molecule can be observed, with the formation of a new paramagnetic species assignable to superoxide radical anions, O_2^-. The EPR spectra recorded after contacting with oxygen are reported in figure 5. In the case of bare ZnO (trace a) the detected signal can be ascribed to the superoxide anion adsorbed on Zn^{2+} cations. Indeed, the computer simulation reported in Fig. $5a_{sim}$ (Panel B) has been performed using a g_{zz} value of 2.051, that is typical for O_2^- absorbed on Zn^{2+} and already reported in literature [24]. Table 2 reports all the parameters obtained from the spectra computer simulations. Spectra b and c, related to the sample containing respectively 1% and 10% of cerium, seem to be more complex. The chemistry of superoxide adsorbed on ceria has been thoroughly described in a paper by J. C. Conesa and

coworkers [25] who specifically adopt this reactivity as a tool to investigate the level of defects of the surface of the oxide. It is well known that bare CeO_2 easily loses and reincorporates oxygen under reductive and oxidative conditions respectively. This redox cycle occurs in the conditions of catalytic processes. The spectrum related to CZ10 (Fig. 5c) shows the already reported [26] typical features of superoxide ions at the surface of CeO_2. The computer simulation reported in Fig. $5c_{sim}$ have been obtained using the following values for the g tensor elements: $g_{zz} = 2.036$, $g_{yy} = g_{xx} = 2.011$ (Table 2), where the z direction corresponds to the oxygen internuclear axis. The value of the high field component is quite anomalous because is at $g_{xx} = 2.011$, instead of having the free spin value ($g_e = 2.0023$) expected in terms of the ionic model of adsorbed superoxide [24], very close to g_{yy}, producing an unresolved perpendicular line. This anomalous value of g_{xx} shown by superoxide ions on cerium dioxide has already been discussed (Conesa , M. Che, J. F. J. Kibblewhite, A. J. Tench, M. Dufaux and C. Naccache, J. Chem. Soc., Faraday Trans. 1, 1973, 69, 857–863) in terms of a model involving some degree of covalence in the interaction of adsorbed oxygen with the 4f cerium orbitals and causing deviations from the purely ionic model. Even if present only for the 10%, cerium oxide seems to dominate the redox chemistry of the system. The spectrum in Fig. 5b (CZ1) is more complex and can be interpreted in terms of the superposition of two distinct signals, namely that of O_2^- on Zn^{2+} and that of O_2^- on Ce^{4+}. According to the computer simulation, the spectrum in Fig.5b panel B is the result of the overlap of the two spectra in Fig 5a and 5c thus indicating an intermediate behaviour of the low Ce loading material. The described spectra are similar to those reported by Coronado et al. [27] that were obtained in the case of a mixed material based on CeO_2–TiO_2 sample with a low cerium loading (0.5%), analogous to that studied in our case. [C6]

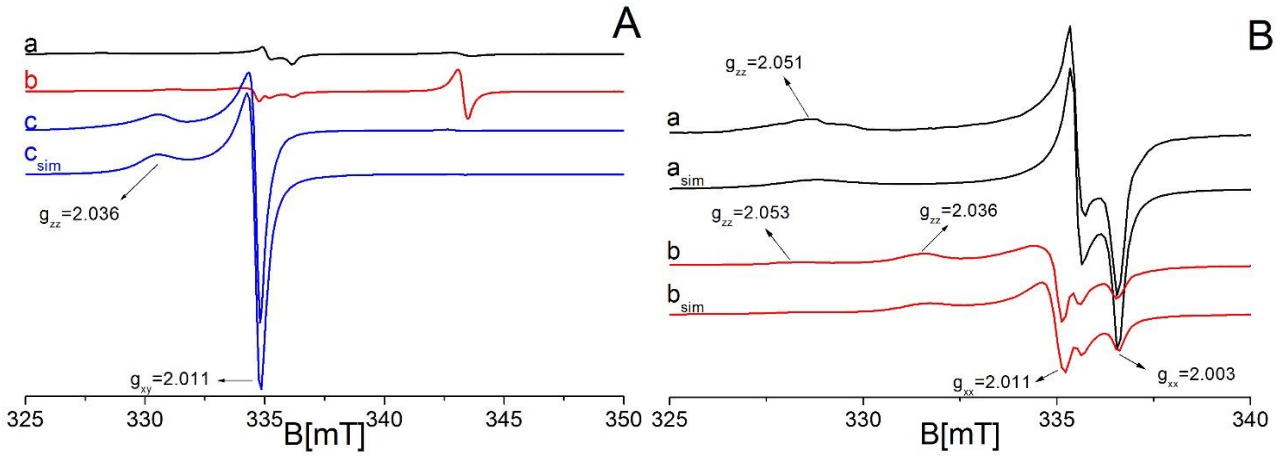

Figure 5. EPR spectra of superoxide species on Panel A: a) ZnO, b) CZ1, c) CZ10. Panel B is a magnification of ZnO and CZ1 spectra with their computer simulation.

Table 2: EPR parameters (g values) of superoxide species for all the samples

Sample	Abundance	g_{zz}	g_{yy}	g_{xx}	ref
ZnO	1	2.0506±0.0001	2.0092±0.0001	2.0027±0.0001	This work
CZ1	0.51	2.0531±0.0001	2.0089±0.0001	2.0026±0.0001	This work
	0.48	2.0365±0.0001	2.0116±0.0001	2.0116±0.0001	
CZ10	1	2.0365±0.0001	2.0116±0.0001	2.0112±0.0001	This work
CeO_2	1[C7]	2.030	2.010	2.010	[28]

3.2 Photoactivity and photochemical properties

The potential photo-activity of the materials was tested irradiating an aqueous suspension of the various solids with the polychromatic light emitted by a Xe lamp bearing a cut off filter at 420nm and using DMPO (5,5-dimethyl-1-pyrroline-N-oxide) as spin trapping agent to detect the formation of hydroxyl radicals ($OH^{\bullet}$) in solution. The DMPO molecule (diamagnetic) forms a stable paramagnetic adduct with OH radicals (DMPO/$OH^{\bullet}$), detectable by the EPR technique [29]. The hydroxyl radicals are important, being responsible for the oxidative degradation of organic molecules in photocatalytic reactions. They are formed under irradiation according to the following process:

$$h^{+}_{(VB)} + H_2O \rightarrow HO^{\bullet} + H^{+}$$

As expected the aqueous suspension of pristine ZnO does not form an appreciable amount of OH radicals under visible irradiation while doped samples are active. Figure 6 (panel A) reports indeed the classic four-lines EPR spectra of the DMPO/$OH^{\bullet}$ adduct, as observed after 60 minutes of irradiation. This time roughly corresponding to the maximum intensity reached by the EPR spectra, and consequently to the higher amount of hydroxyl groups generated. Panel B reports the integrated values of the EPR spectra (which are proportional to the radical concentration present in solution) as a function of the irradiation time. Both doped samples are photoactive under visible light and the production of OH radical reaches its maximum value between 30 min and 60 min. In particular, the activity is proportional to the Ce loading and the CZ10 sample clearly results more active if compared to the CZ1 one.

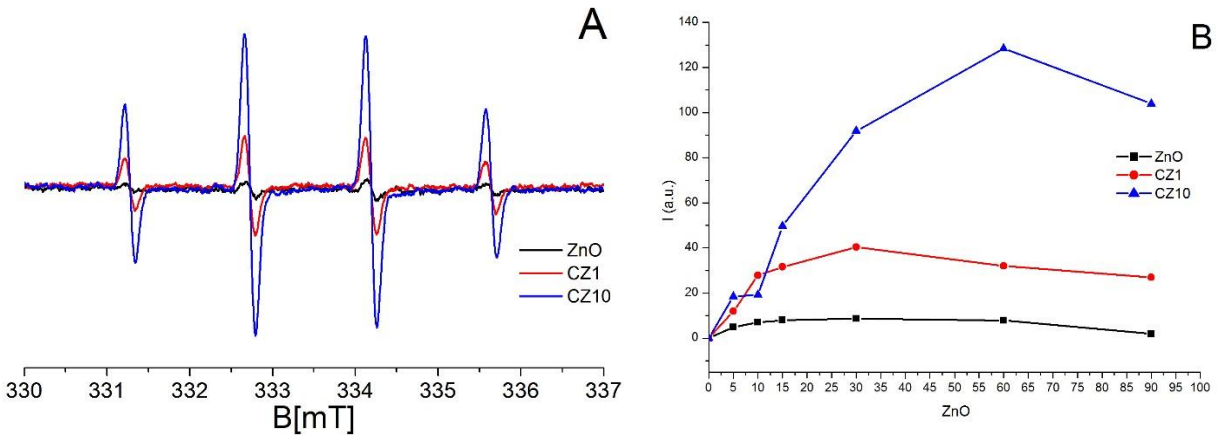

Figure 6. Panel A: EPR spectra of the DMPO/OH• adduct produced by irradiation of an aqueous suspension of the three samples ZnO, CZ1 and CZ10 with visible/NIR light (λ>420nm); Panel B: Integrated intensities of the EPR spectra as a function of irradiation time.

Conclusions

Zinc oxide and cerium dioxide have no or little propensity to form solid solutions. When prepared by co-precipitation from a solution containing Zn and Ce ions, a solid with two independent phases of the two oxides is formed, as indicated by XRD. The optical properties of the mixed systems (with Zn:Ce molar ratio of 0.01:1 and 0.1:1) are those of ZnO (band gap around 3.2-3.3 eV) with the onset of a broad absorption from 370nm to 450 nm due to the presence of CeO_2 phase. The latter phase decorates the surface of ZnO as indicated by a clear role of cerium in the surface chemistry of the mixed systems (Fig.5). Reductive annealing of the solid and successive contact with oxygen in fact lead to the formation of superoxide anions that are exclusively adsorbed on Ce^{4+} surface ions (high Ce loading sample) or shared by Ce^{4+} and Zn^{2+} surface sites (low Ce loading). The interaction between the two phases however produces an interesting photochemical effect: the presence of cerium sensitizes the system to visible light. Irradiation in fact generates electron-hole pairs and the holes form, as well established, reactive OH radical detected by spin trapping EPR. The mixed systems have therefore a potential photocatalytic activity under visible light. The detailed mechanism of photo-activation is presently under investigation in our laboratory. The presence of cerium brings about absorption of visible photons (Fig. 2) but probably also contributes subtracting part of the photo-generated electrons using Ce^{4+}/Ce^{3+} pairs thus limiting the effect of electron-hole recombination that is detrimental to photo-activity.

References

References

[1] P. Li, Z. Wei, T. Wu, Q. Peng, Y. Li, Au-ZnO Hybrid Nanopyramids and Their Photocatalytic Properties, J. Am. Chem. Soc., 133 (2011) 5660-5663.
[2] H. Fu, S.-W. Tsang, Infrared colloidal lead chalcogenide nanocrystals: Synthesis, properties, and photovoltaic applications, Nanoscale, 4 (2012) 2187-2201.
[3] H. Cheun, C. Fuentes-Hernandez, Y. Zhou, W.J. Potscavage, Jr., S.-J. Kim, J. Shim, A. Dindar, B. Kippelen, Electrical and Optical Properties of ZnO Processed by Atomic Layer Deposition in Inverted Polymer Solar Cells, J. Phys. Chem. C, 114 (2010) 20713-20718.
[4] X. Zou, H. Fan, Y. Tian, S. Yan, Facile hydrothermal synthesis of large scale ZnO nanorod arrays and their growth mechanism, Mater. Lett., 107 (2013) 269-272.
[5] U. Özgür, Y.I. Alivov, C. Liu, A. Teke, M.A. Reshchikov, S. Doğan, V. Avrutin, S.J. Cho, H. Morkoç, A comprehensive review of ZnO materials and devices, J. Appl. Phys., 98 (2005) 041301.
[6] C.-J. Chang, C.-Y. Lin, M.-H. Hsu, Enhanced photocatalytic activity of Ce-doped ZnO nanorods under UV and visible light, J. Taiwan Inst. Chem. Eng., 45 (2014) 1954-1963.
[7] M. Ahmad, E. Ahmed, F. Zafar, N.R. Khalid, N.A. Niaz, A. Hafeez, M. Ikram, M.A. Khan, Z. Hong, Enhanced photocatalytic activity of Ce-doped ZnO nanopowders synthesized by combustion method, Journal of Rare Earths, 33 (2015) 255-262.
[8] Y.Q. Zong, Z. Li, X.M. Wang, J.T. Ma, Y. Men, Synthesis and high photocatalytic activity of Eu-doped ZnO nanoparticles, Ceram. Int., 40 (2014) 10375-10382.
[9] Y. Zong, Z. Li, X. Wang, J. Ma, Y. Men, Synthesis and high photocatalytic activity of Eu-doped ZnO nanoparticles Ceram. Int., 40 (2014).
[10] W.K. Tan, K.A. Razak, Z. Lockman, G. Kawamura, H. Muto, A. Matsuda, Photoluminescence properties of rod-like Ce-doped ZnO nanostructured films formed by hot-water treatment of sol-gel derived coating, Opt. Mater., 35 (2013) 1902-1907.
[11] S. Anandan, A. Vinu, T. Mori, N. Gokulakrishnan, P. Srinivasu, V. Murugesan, K. Ariga, Photocatalytic degradation of 2,4,6-trichlophenol using lanthanum doped ZnO in acqueous suspension, Catal. Commun., 8 (2007).
[12] M.C. Paganini, D. Dalmasso, C. Gionco, V. Polliotto, L. Mantilleri, P. Calza, Beyond TiO2: Cerium-Doped Zinc Oxide as a New Photocatalyst for the Photodegradation of Persistent Pollutants, ChemistrySelect, 1 (2016) 3377-3383.
[13] C.M. Teh, A.R. Mohamed, Roles of titanium dioxide and ion-doped titanium dioxide on photocatalytic degradation of organic pollutants (phenolic compounds and dyes) in aqueous solutions: A review, J. Alloys Compd., 509 (2011) 1648-1660.
[14] E.D. Sherly, J.J. Vijaya, L.J. Kennedy, Effect of CeO_2 coupling on the structural, optical and photocatalytic properties of ZnO nanoparticle, J. Mol. Struct., 1099 (2015) 114-125.
[15] G. He, H. Fan, Z. Wang, Enhanced optical properties of heterostructured ZnO/CeO_2 nanocomposite fabricated by one-pot hydrothermal method: Fluorescence and ultraviolet absorption and visible light transparency, Opt. Mater., 38 (2014) 145-153.
[16] C.-h. Zeng, S. Xie, M. Yu, Y. Yang, X. Lu, Y. Tong, Facile synthesis of large-area CeO_2/ZnO nanotube arrays for enhanced photocatalytic hydrogen evolution, J. Power Sources, 247 (2014) 545-550.
[17] C. Gionco, M.C. Paganini, E. Giamello, R. Burgess, C. Di Valentin, G. Pacchioni, Cerium-Doped Zirconium Dioxide, a Visible-Light-Sensitive Photoactive Material of Third Generation, The journal of physical chemistry letters, 5 (2014) 447-451.
[18] Jin-Chung Sina, Sze-Mun Lamb, Keat-Teong Leec, A.R. Mohamed, Preparation of cerium-doped ZnO hierarchical micro/nanospheres with enhanced photocatalytic performance for phenol degradation under visible light, Journal of Molecular Catalysis A, 409 (2015) 1-10.
[19] X. Wang, L. Huang, Y. Zhao, Y. Zhang, G. Zhou, Synthesis of Mesoporous ZnO Nanosheets via Facile Solvothermal Method as the Anode Materials for Lithium-ion Batteries, Nanoscale research letters, 11 (2016) 37.

[20] O. Bechambi, A. Touati, S. Sayadi, W. Najjar, Effect of cerium doping on the textural, structural and optical properties of zinc oxide: Role of cerium and hydrogen peroxide to enhance the photocatalytic degradation of endocrine disrupting compounds, Mater. Sci. Semicond. Process., 39 (2015) 807-816.
[21] G. Martra, E. Gianotti, S. Coluccia, The Application of UV-Visible-NIR Spectroscopy to Oxides, Metal Oxide Catalysis, Wiley-VCH Verlag GmbH & Co. KGaA2009, pp. 51-94.
[22] C. Gonzalez, D. Block, R.T. Cox, A. Hervè, Magnetic Resonance Studies Of Shallow Donors In Zinc Oxide J. Cryst. Growth, 59 (1982).
[23] L.E. Halliburton, N.C. Giles, N.Y. Garces, M. Luo, C. Xu, L.B.A. Boatner, Production of native donors in ZnO by annealing at high temperature Zn vapour, Appl. Phys. Lett., 87 (2005).
[24] M. Che, A.J. Tench, Characterization and Reactivity of Molecular Oxygen Species on Oxide Surfaces advances in catalysis 32 (1983).
[25] J. Soria, A. Martìnez-Arias, J.C. Conesa, Spectroscopic Study of Oxygen Adsorption as a Method to Study Surface Defects on CeO, , Journal of the Chemical Society Faraday Transistor, 91 (1995).
[26] J.C. Conesa, Computer modeling of surfaces and defects on cerium dioxide, Surf. Sci. Rep., 339 (1995) 337-352.
[27] J.M. Coronado, A.J. Maira, A. Martìnez-Arias, J.C. Conesa, J. Soria, EPR study of the radicals formed upon UV irradiation of ceria-based photocatalysts Journal of Photochemistry and Photobiology A, 150 (2002).
[28] L. Mendelovici, H. Tzehoval, M. Steinberg, The adsorption of oxygen and nitrous oxide on platinum ceria catalyst, Applications of surface science, 17 (1983).
[29] D. Dvoranová, V. Brezová, M. Mazúr, M.A. Malati, Investigations of metal-doped titanium dioxide photocatalysts Appl. Catal., B, 37 (2002).

Acknowledgement